The Astrophysical Journal, 932:95 (10pp), 2022 June 20 https://doi.org/10.3847/1538-4357/ac6e3b

Chromospheric Recurrent Jets in a Sunspot Group and Their Intergranular Origin

Jie Zhao[1], Jiangtao Su[2,3], Xu Yang[4,5], Hui Li[1,6], Brigitte Schmieder[7,8,9], Kwangsu Ahn[4,5], and Wenda Cao[4,5]
[1] Key Laboratory of Dark Matter and Space Astronomy, Purple Mountain Observatory, Chinese Academy of Sciences, Nanjing, Jiangsu, People's Republic of China
zhaojie@pmo.ac.cn
[2] Key Laboratory of Solar Activity, National Astronomical Observatories, Chinese Academy of Sciences, Beijing 100012, People's Republic of China
[3] School of Astronomy and Space Science, University of Chinese Academy of Sciences, Beijing 101408, People's Republic of China
[4] Center for Solar-Terrestrial Research, New Jersey Institute of Technology, 323 Martin Luther King Boulevard, Newark, NJ 07102, USA
[5] Big Bear Solar Observatory, New Jersey Institute of Technology, Big Bear City, CA 92314, USA
[6] School of Astronomy and Space Science, University of Science and Technology of China, Hefei 230026, People's Republic of China
[7] LESIA, Observatoire de Paris, Université PSL, CNRS, Sorbonne Université, Université de Paris, 5 place Jules Janssen, F-92195 Meudon, France
[8] Centre for Mathematical Plasma Astrophysics, Department of Mathematics, KU Leuven, B-3001 Leuven, Belgium
[9] SUPA, School of Physics & Astronomy, University of Glasgow, Glasgow G12 8QQ, UK
Received 2022 January 24; revised 2022 April 6; accepted 2022 May 7; published 2022 June 20

Abstract

We report on high-resolution observations of recurrent fan-like jets by the Goode Solar Telescope in multiple wavelengths inside a sunspot group. The dynamics behavior of the jets is derived from the Hα line profiles. Quantitative values for one well-identified event have been obtained, showing a maximum projected velocity of 42 km s^{-1} and a Doppler shift of the order of 20 km s^{-1}. The footpoints/roots of the jets have a lifted center on the Hα line profile compared to the quiet Sun, suggesting a long-lasting heating at these locations. The magnetic field between the small sunspots in the group shows a very high resolution pattern with parasitic polarities along the intergranular lanes accompanied by high-velocity converging flows (4 km s^{-1}) in the photosphere. Magnetic cancellations between the opposite polarities are observed in the vicinity of the footpoints of the jets. Along the intergranular lanes horizontal magnetic field around 1000 G is generated impulsively. Overall, all the kinetic features at the different layers through the photosphere and chromosphere favor a convection-driven reconnection scenario for the recurrent fan-like jets and evidence a site of reconnection between the photosphere and chromosphere corresponding to the intergranular lanes.

Unified Astronomy Thesaurus concepts: Solar photosphere (1518); Solar magnetic fields (1503); Solar chromosphere (1479)

1. Introduction

Recurrent fan-like jets that appear like a chain of eruptions from one end to another in the high-resolution chromosphere observations are the prevalence of a highly dynamic behavior. Due to the limitation of spatial resolution, they have been named as Hα surges, plasma ejections, and chromospheric jets (such as in Roy 1973; Asai et al. 2001; Louis et al. 2014). With the recent high-resolution observations, they have also been named light walls (Yang et al. 2015) or peacock jets (Robustini et al. 2016). Among such phenomena, the one that happens inside the umbra in light bridge (LB) has attracted more attention. The oscillations of fan-like jets (plasma ejections/surges) inside a sunspot LB were first reported in Asai et al. (2001) with Hα observations by the Domeless Solar Telescope at Hida Observatory and 171 Å observations from the Transition Region and Coronal Explorer (TRACE; Handy et al. 1999). The main characteristics of these jets were defined by their velocity around 50 km s^{-1} and their maximum length of 2 Mm. Emerging magnetic flux was considered to be the origin of the jets with no strong observational evidence.

Observed in multiple wavelengths throughout the solar atmosphere, fan-like jets have been extensively studied in recent years (see the reviews of Tian et al. 2018; De Pontieu et al. 2021; Schmieder et al. 2021). They are identified in high spatial resolution observations, such as in Hα and transition region lines observed with the Interface Region Imaging Spectrograph (IRIS; De Pontieu et al. 2014) with different morphologies (velocity, maximum height, period). They appear as dark features in Hα images with a bright front in the transition region and coronal lines (such as in Yang et al. 2015). The jets occur not only above LB but also above magnetic neutral lines (Hou et al. 2016), with trigger of magnetoacoustic waves (Zhang et al. 2017), magnetic reconnection (Hou et al. 2017; Bai et al. 2019; Yang et al. 2019b), or a combination of both mechanisms (Tian et al. 2018). They may also be associated with vortex flows (Yang et al. 2019a).

The magnetoacoustic wave origins are predominantly identified from the periodic behavior of the jet oscillations or of the displacements of the bright front, while the magnetic reconnection origins are confirmed from the high-resolution observations of magnetic field. With the Hinode spectro-polarimeter (SP; Ichimoto et al. 2008; Lites et al. 2013), Shimizu et al. (2009, hereafter S09) found that a trapped flux tube beneath the canopy magnetic field is responsible for long-lasting chromospheric plasma ejections. The interaction of magnetic field between the LB and the surroundings is also suggested to raise the local dynamic (Louis et al. 2014; Toriumi et al. 2015b).

Simulations of jets, such as X-ray jets (Shimojo & Shibata 2000), surges (Yokoyama & Shibata 1996), solar polar jets (Pariat et al. 2009), active region recurrent jets (Archontis et al. 2010), and microflare accompanying jets (Jiang et al. 2012), show different physical processes, but all are associated

with magnetic field changes. Takasao et al. (2013) simulated flux-emergence-associated chromospheric jets and displayed two possible scenarios with different reconnection heights. With a lower reconnection site, such as that in the photosphere, a slow-mode shock propagates and lifts up the transition region, forming the so-called jets. With a higher reconnection site, such as that in the upper chromosphere, Lorentz force and the whip-like motion of magnetic field accelerate the chromospheric plasma. Since the jets originate from the LB in some cases, Toriumi et al. (2015a, hereafter T15) did a detailed analysis of such structures with the MURaM simulation of flux emergence in an active region. Their results show that the convective upflow transport horizontal field to the solar surface, configuring LB structure, and the jet-associated magnetic reconnection happen as a result of the magnetic shear between the horizontal field of the LB and the ambient vertical field in the sunspot. The morphology, magnetic field, and convective velocity near the solar surface are compared between the Hinode observations and MHD simulations around the LB, which shows a good correspondence.

Although previous observations have shown the intimate relation between the fan-like jets and the photospheric magnetic field, the spatial resolution is limited to subseconds, such as $0\farcs3\,\mathrm{pixel}^{-1}$ of Hinode/SP, and a detailed comparison between different layers is rarely achieved. With the aid of extremely high resolution observations from the Goode Solar Telescope (GST; Cao et al. 2010), we associate the chromospheric plasma eruptions with the photospheric granule movements and the intergranular magnetic field. Our paper is organized as follows: In Section 2, we list the observations that we investigated in this work and the inversion method adopted for obtaining the magnetic field. The results are shown in Section 3, and we discuss our conclusions in Section 4.

2. Observations and Data Reduction

Intermittently recurrent fan-like jets that happened in between the well-developed east sunspot of NOAA Active Region 12585 (N07°, W25°) were observed in multiple wavelengths with GST at the Big Bear Solar Observatory (BBSO) on 2016 September 7.

The Hα images are observed by the Visible Imaging Spectrometer (VIS; Cao et al. 2010), with a scanning wavelength step 0.02 nm from −0.12 to 0.12 nm of the line center. The pixel size is $0\farcs029$, with an effective temporal resolution of 33 s for every single wavelength.

The TiO images at 705.7 nm are observed by the Broadband Filter Imager (BFI; Cao et al. 2010), with a bandpass of 1 nm, showing the photospheric counterpart of the jets. The temporal resolution is 30 s, and the pixel size is $0\farcs034$.

The full-Stokes Near InfraRed Imaging Spectropolarimeter (NIRIS; Cao et al. 2012; Ahn et al. 2016; Ahn & Cao 2019) observes the photospheric line of Fe I 1564.85 nm for magnetic Stokes profiles, with a pixel size of $0\farcs083$. There are 40 spectral sampling positions from −0.316 to 0.31 nm with respect to the line center, and the cadence is around 73 s for vector magnetic field.

For the inversion of magnetic field and other parameters from the Stokes profiles, a Milne−Eddington atmosphere is assumed, such as the one in Wang et al. (2017), and a minimum-energy approach (Leka et al. 2009a, 2009b) is adopted to resolve the 180° ambiguity in the azimuth angle of the vector magnetic field.

For the alignment of images in different wavelengths, the TiO images are rotated and shifted with respect to the continuum image of the Helioseismic and Magnetic Imager (HMI; Scherrer et al. 2012), and then the images of Stokes profiles and Hα far wings are co-aligned with the TiO images, and finally the Hα near-line-center images are co-aligned with the Hα far-wing images. We show the result after co-alignment (all north-up) at one time step in Figure 1 when the jet is apparent in the field of view (FOV), which covers a region of $60'' \times 60''$. The photospheric image in TiO band and the HMI continuum image are displayed in the top panels, and the chromospheric responses in the red wings of Hα are shown in the bottom panels. The fan-like jets are apparent in between the sunspots and have been annotated with blue curves along the ejection trajectory.

3. Results

3.1. Chromospheric Jets

To investigate the temporal evolution of the fan-like jets, we consider the intensity at Hα line center and wings along the blue curve in Figure 1 stacked over time and the time–distance maps shown in Figure 2. A time range of 17:00 UT–17:44 UT is selected considering the overlap of the multiwavelength observations and the data quality.

Fan-like jets appear as dark features in the time–distance map while the background of the chromosphere is bright. The intensity fluctuation of the jets indicates upward movements in the blue wings (H$\alpha-0.6$, 0.8, 1.0 Å), and the downward movements can also be identified in the red wings (H$\alpha+0.6$, 0.8, 1.0 Å). Nevertheless, the dark plasma jets are less intense in the far wings of H$\alpha\pm0.8$ and 1.0 Å, especially in the blue wing, which manifests asymmetric distribution of the upward and downward movement of the jets at high speed. One of the recurrent jets that can be clearly identified from the time–distance map of H$\alpha\pm0.8$ and 1.0 Å has been selected, and its trajectory has been fitted with a parabolic profile following the method used in Robustini et al. (2016). The averaged projected velocity is then estimated to be $42\,\mathrm{km\,s^{-1}}$. For the remaining ejections, most of them cannot be well established owing to the blend of the upflow with downflow.

Two points of A and B on the slice are selected and marked with a horizontal white solid line and black dashed–dotted line in Figure 2 to represent the jets and the chromospheric roots, respectively. The two crossing points of the white horizontal line and the parabolic profile are marked with white plus signs to represent the times when upflow (at time T1) and downflow (at time T2) are passing through point A consecutively during the selected jet event. The red plus sign at the first crossing point of the dashed–dotted line and the parabolic profile is annotated to show the time (T0) when the root is intimately associated with the selected jet event and is investigated later. Examples of temporal evolution of the Hα intensity from the blue wing to the red wing along the aforementioned two horizontal lines are stacked and displayed in Figure 3. The top panel shows the result for the fan-like jets; the bottom panel, for the root. The wavelength in the vertical axis is displayed in the format of Doppler velocity, which is calculated with $v=(\delta\lambda/\lambda_0)\cdot c$, where λ_0 is the line-center wavelength of Hα and $\delta\lambda$ is the offset to the line center. In general, an intermittent event can be found in both panels, while no correspondence can be related to most of the fan-like jets and the root. This is

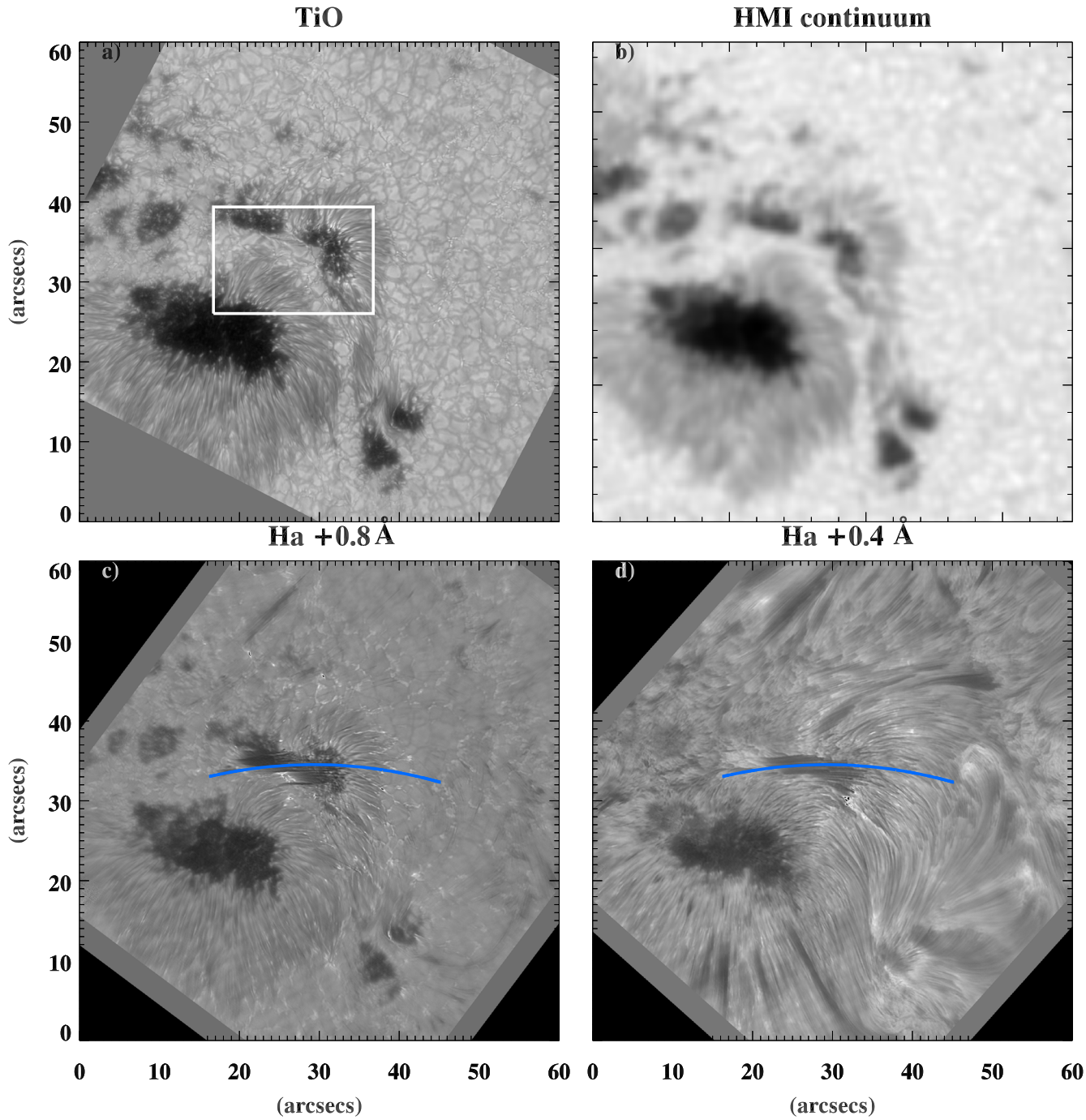

Figure 1. Overview of the co-aligned observations of AR12585: (a) TiO white-light (705.7 nm) image from GST/BFI; (b) SDO/HMI continuum (617.3 nm) image; chromospheric images observed in (c) Hα + 0.8 Å and (d) Hα + 0.4 Å by GST/VIS. All the images from GST are rotated and co-aligned with the HMI continuum image. The white rectangle in the TiO image shows an FOV displayed in Figures 5 and 6. The recurrent fan-like jets are identified from the chromospheric images in the bottom panels, and their trajectories are annotated with blue curves.

probably due to the mixture of the jets between two consecutive eruptions, i.e., the coordinated upflow and downflow, which also complicate the Doppler velocity distribution. The dark feature of the fan-like jets and the root is mainly located in between $\pm 30\,\mathrm{km\,s^{-1}}$ (white dotted lines), showing a recurrent blueshift-to-redshift pattern. The identified jet event in Figure 2 is also marked with a dotted line in the top panel, with T1 and T2 showing the times when the upflow and downflow pass through point A during the jet event. The Doppler velocity shows a response in all the blue wings of Hα at the same time, while the response in the red wing appears consecutively from the near line center to the far wings. The result of the rapid blueshift followed by a slowly increasing redshift is the manifestation of the so-called magnetoacoustic shock waves (e.g., Su et al. 2016). The time (T0) when the root of the selected jet is studied is also marked with a red plus sign as in Figure 2 and a vertical line in the bottom panel.

The normalized Hα line profiles at time T0 for the chromospheric root and quiet region and at times T1 and T2 for the jet are shown in Figure 4. The plus signs with different colors show the observed data sets for different features, while the curves show the fitting results. The line centers from the fitted results are labeled

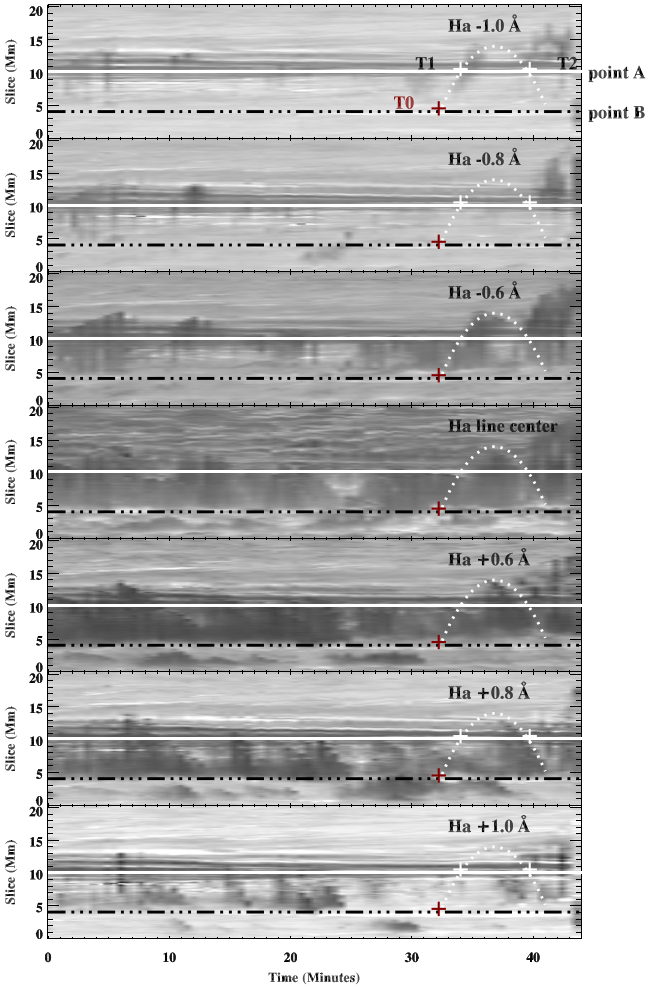

Figure 2. Time–distance plots that sample the recurrent fan-like jets along the blue curve in Figure 1 are displayed with a time range from 17:00 UT to 17:44 UT. Evolution in the wavelengths from Hα − 1.0 Å to Hα + 1.0 Å is shown from top to bottom. One jet event has been selected and outlined with white dotted parabolic lines. Points A and B, which are annotated with a white line and black dashed–dotted line, are selected to represent a point in the jet and the root, respectively. The white plus signs in the top and bottom panels show the times (T1 and T2) when upflow and downflow, which are mainly observed in H$\alpha \pm 0.8$ Å and ± 1.0 Å, are passing through point A, respectively. The red plus sign in all panels shows the time (T0) when the root of the selected jet event is investigated later. Examples of the intensity evolution at points A and B of Hα from the blue wing to the red wing with a wavelength step of 0.2 Å are stacked and displayed in Figure 3.

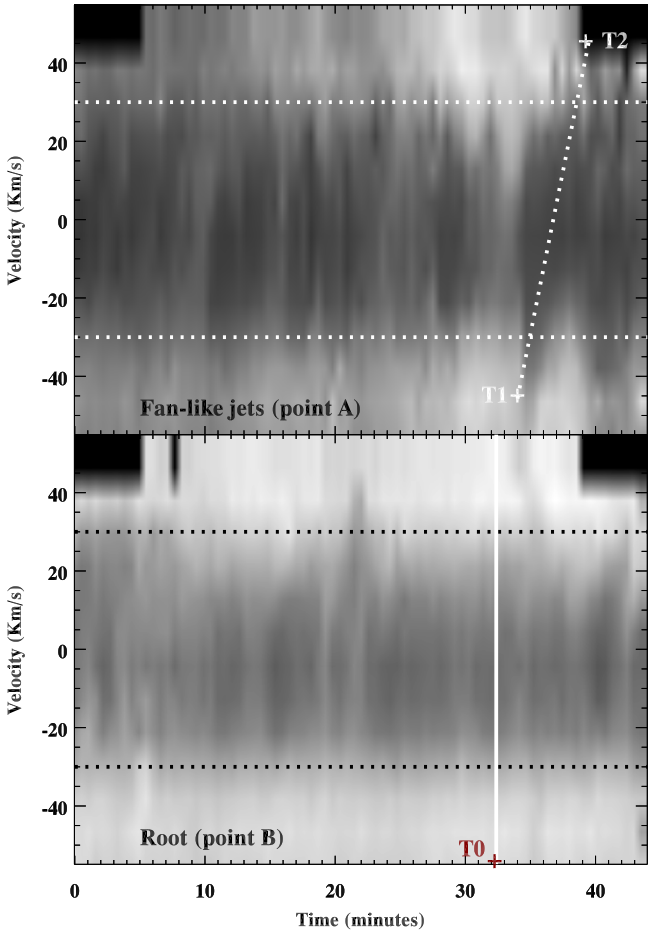

Figure 3. Temporal evolution of stacked Hα intensity from the blue wing to the red wing for point A on the path of the fan-like jets (top panel) and point B of the root (bottom panel). Different wavelengths along the vertical axis have been transformed into Doppler velocity, and the ones of ± 30 km s^{-1} are annotated with dotted horizontal lines for reference. The oblique dotted line in the top panel demonstrates the same jet event, and the white plus signs at the two ends mark the same times (T1 and T2) as demonstrated in Figure 2. Both the vertical white line and the red plus sign in the bottom panel show the time (T0) when the intensity profile of the root is displayed in Figure 4. Dark blocks at the corners exist owing to the missing observations at the Hα far wing in red.

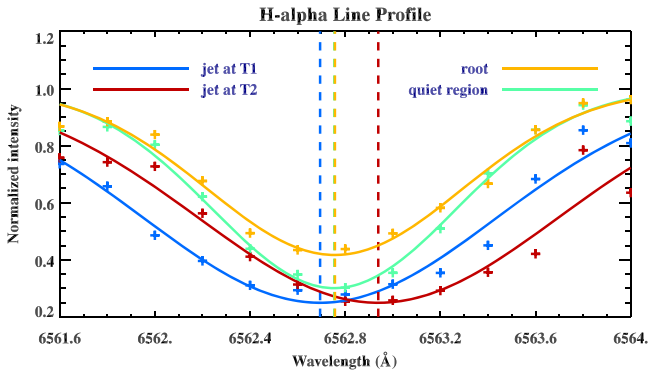

Figure 4. Normalized intensity profiles vs. wavelengths for the jet (at T1 and T2), the root (at T0), and the quiet region (at T0). The plus signs show the observed data sets, and the solid curves show the fitting results. The vertical dotted lines give the line center from the fitted curves.

with vertical lines. The line profile at the chromospheric quiet region (green line) shows a blueshift that corresponds to a velocity around 2 km s^{-1} if the line center of Hα is assumed to be 6562.8 Å. The Hα line center of the jet shows a blueshift at T1 ($\sim$3 km s^{-1}) and a redshift at T2 ($\sim$8 km s^{-1}), while that of the root (yellow profile) does not show apparent Doppler shift, both relative to the quiet region. A cloud model analysis following the formula of Schmieder et al. (1988) may lead to higher Doppler shifts for the jet at times T1 and T2 of the order of 15−20 km s^{-1}, giving an estimation of the inclination of the jet versus the vertical $\sim$60°. Comparing with the quiet region, less absorption is found around the line center for the root, while more absorption is found for the jet, which means that the root might be heated while the jet is dominated with cold plasma without apparent heating. Although less absorption of Hα does not always mean local heating, it is indeed a manifestation of the reconnection that happens in between the photosphere and chromosphere in this study, which is approved later and considered to be responsible for the recurrent jets.

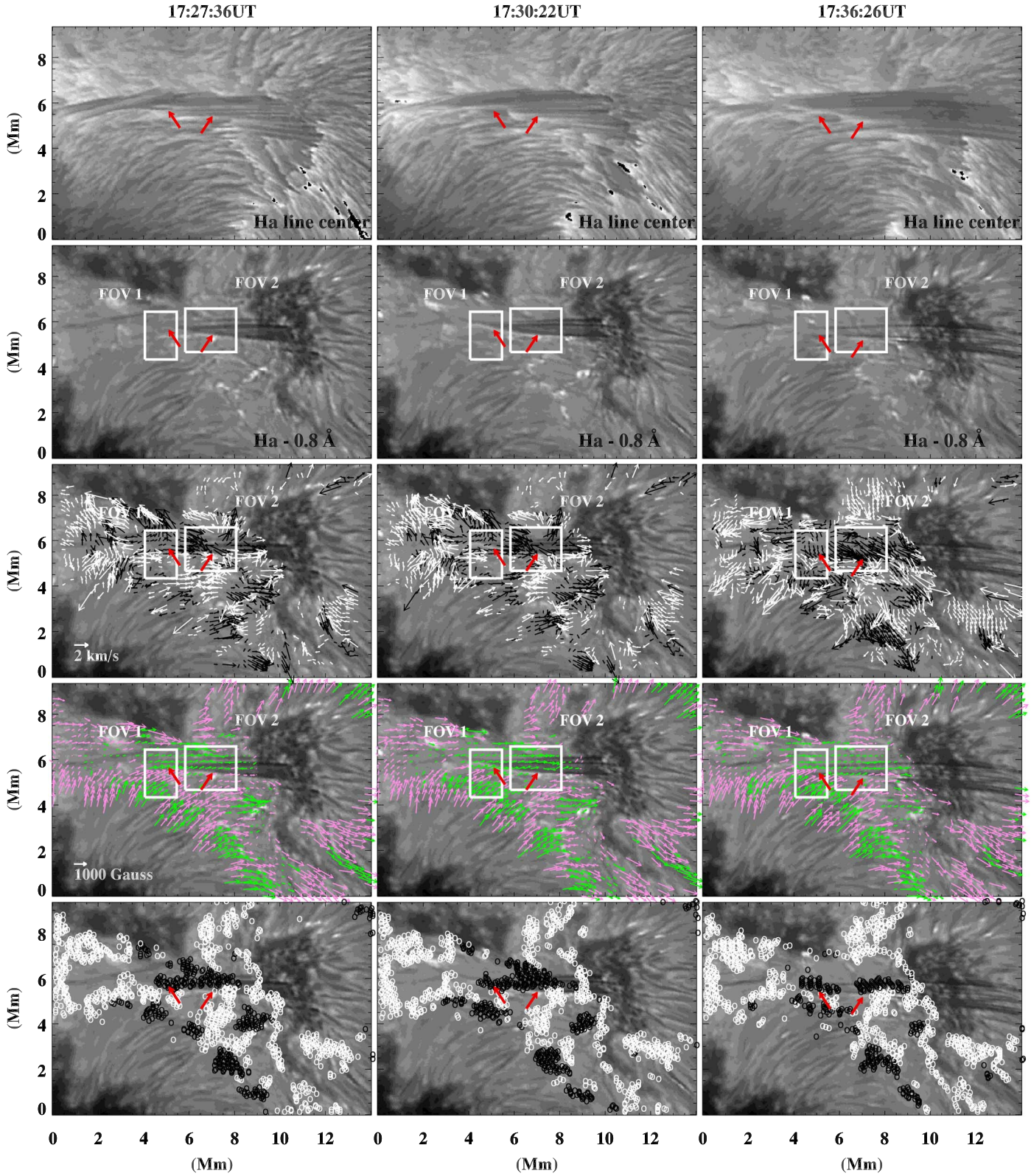

Figure 5. The images of Hα line center (first row) and Hα − 0.8 Å (bottom four rows) at three different times are displayed from left to right; different features are overlaid on the Hα − 0.8 Å images in the bottom three rows. Third row: the surface (horizontal) velocity at photosphere is overlaid with arrows, and white and black colors correspond to velocity with positive and negative B_l, respectively. Fourth row: the horizontal magnetic field is overlaid with arrows, while pink and green colors corresponds to B_h with positive and negative B_l, respectively. Fifth row: the longitude magnetic field in the range of 100–800 G with B_h less than 1000 G is overlaid with circles, and white and black colors show positive and negative B_l, respectively. The red arrows indicate the locations of opposite polarities that correspond to the intergranular lanes in Figure 6; the white boxes marked with FOV1 and FOV2 show the places where the magnetic field is investigated (see Section 3.4).

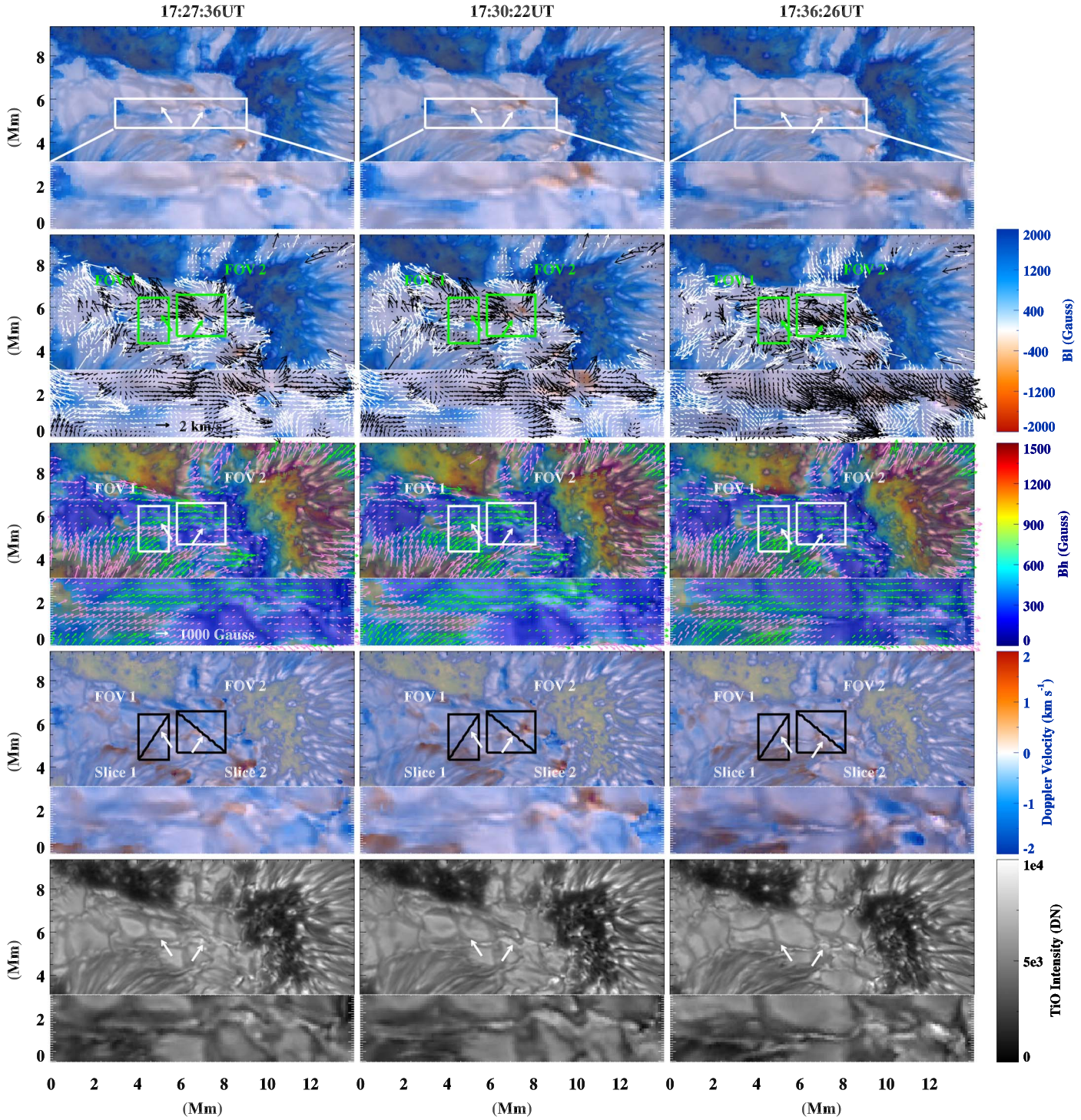

Figure 6. Composite images of TiO with LOS magnetic field (B_l; first two rows), horizontal magnetic field (B_h; third row), and Doppler velocity ($V_{\rm Dop}$; fourth row) are displayed in the top four rows, while the TiO images are displayed in the bottom row for comparison. The evolution at the same time steps as in Figure 5 is shown from left to right. The FOV in the white rectangle as shown in the first row is enlarged, and the zoom-in is displayed for each panel at its bottom.The color bars on the right-hand side, which are for the three parameters B_l, B_h, and $V_{\rm Dop}$, are displayed in the case of zero transparency. Surface velocity and horizontal magnetic field are overlaid as arrows on the images of B_l and B_h in the second and third row, respectively. The colors of arrows have the same meaning as shown in Figure 5. Slice 1 and Slice 2 at the diagonal of FOV1 and FOV2, respectively, show the places where time–distance maps in Figures 7 and 8 are done, and the rectangles of FOV1 and FOV2 show the regions where the parameters in Figure 9 are calculated. The white arrows (green in second row) mark the locations of intergranular lanes as shown in Figure 5.

To investigate the photospheric origins of the fan-like jets, a subregion (white rectangle in Figure 1) was selected. The images of Hα line center (top row) and line wing at Hα − 0.8 Å (bottom four rows) at three time steps around the selected jet event shown in Figures 2 and 3 are displayed in Figure 5. Different features of surface velocity, horizontal magnetic field, and longitude magnetic field are overlaid on the Hα −0.8 Å images in the bottom three rows, respectively. In the top two rows, the recurrent jets are found to have originated from the same places, and two regions of FOV1 and FOV2 as labeled in

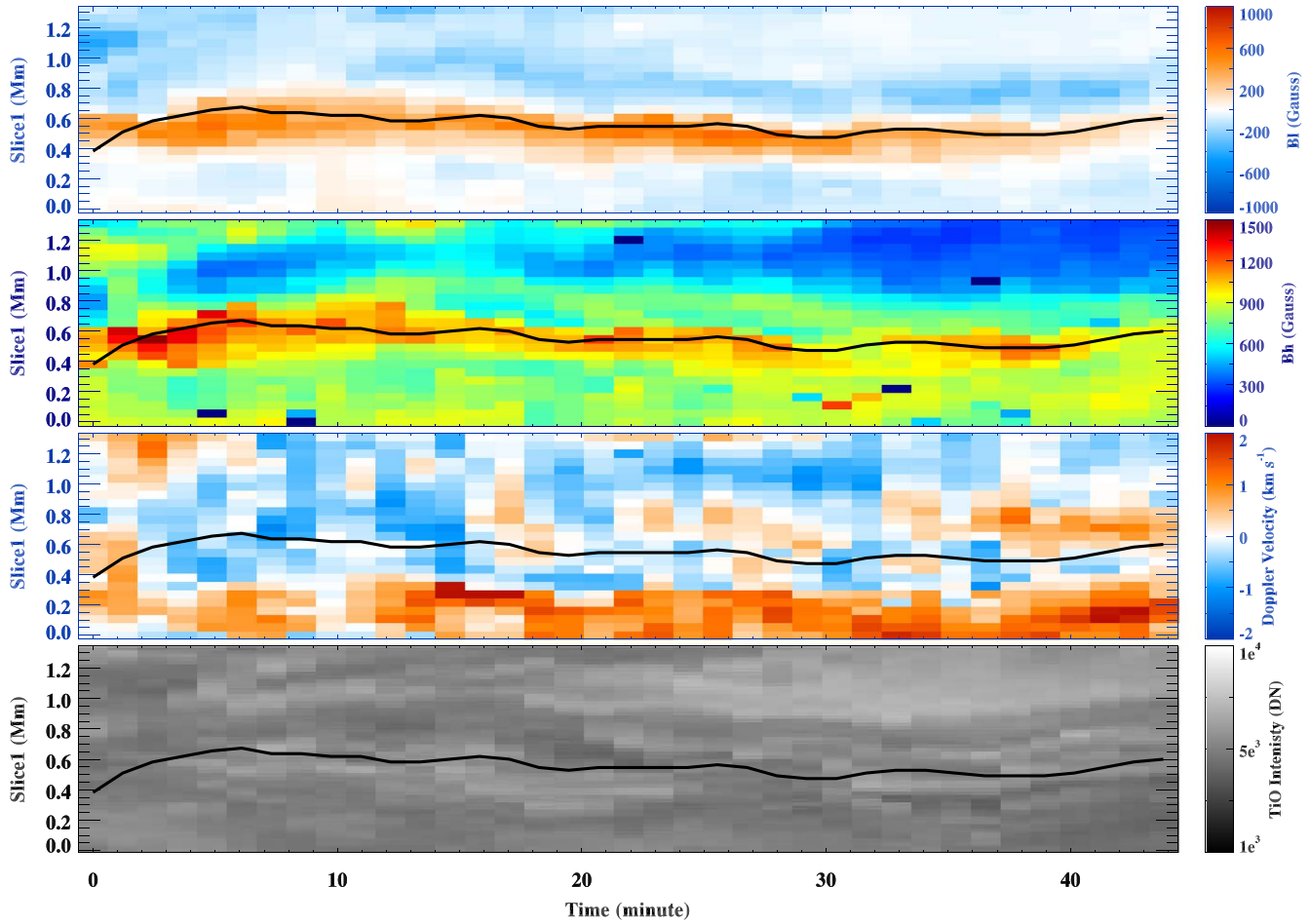

Figure 7. Time–distance images of different parameters at Slice 1. From top to bottom: longitude magnetic field, horizontal magnetic field, Doppler velocity, and TiO intensity. The black curve is obtained by selecting the maximum horizontal field at each time step and is plotted on the other three panels for reference.

the middle three rows are selected for investigation later. The red arrows in each panel show the locations of opposite polarities that correspond to the intergranular lanes in Figure 6. The white and black arrows in the third row show the surface flows in between the magnetic polarities that are obtained from TiO images with the local correlation tracking (LCT) method, and their colors represent surface flow with positive and negative B_l, respectively. Convective flows larger than 2 km s^{-1} (with maximum around 4 km s^{-1}) exist in FOV2, while flows in FOV1 are relative small. An enlargement of the above velocity can also be found in the zoom-in plot in Figure 6, in which the converging motions to the intergranular lanes are identified at some places in the vicinity of the roots. Such flows may help to squash the magnetic field of opposite polarities and trigger the magnetic reconnection. The horizontal magnetic field B_h, which is smaller than 1200 G with B_l less than 1000 G, has been overlaid on the fourth row, and the longitude magnetic field B_l, which has an absolute value in the range of 100–800 G with B_h less than 1000 G, has been overlaid on the fifth row. The former one is represented with arrows (the pink and green colors show B_h with positive and negative B_l, respectively), and the latter one is shown with circles (white and black represent positive and negative B_l, respectively). The magnetic field around the footpoints shows opposite polarities of B_l, which strongly indicates a magnetic field origin for the jets. A detailed description of the obtained magnetic field is shown in Section 3.2.

3.2. Magnetic Fields and Doppler Velocity from Inversion

The photospheric vector magnetic field and the Doppler velocity are obtained through inversion of Fe I Stokes profiles. Their composite images with TiO are shown in the top four rows of Figure 6, while the TiO images are displayed in the bottom row for comparison. The images have the same FOV as in Figure 5, and temporal evolution corresponding to the displayed time steps in Figure 5 is shown from left to right. An enlargement of the FOV in the white rectangle labeled in the first row is displayed for each panel at its bottom part.

In general, at the region in between the sunspots with same positive polarity, the magnetic field is complex. At the outer side of the penumbra of the main pore at the left corner, the horizontal field B_h is around 1000 G and the longitudinal magnetic field B_l shows a mixed pattern of positive and negative. The Doppler velocity shows redshift that is the manifestation of the Evershed downflow. At the rest place in between the sunspots, the absolute value of the longitudinal magnetic field B_l is less than 100 G and the horizontal field B_h is less than 300 G, with absolute value of Doppler velocity less than 0.5 km s^{-1} at most places. However, a relatively strong magnetic field of B_l and B_h, surface convective flow as fast as 4 km s^{-1}, and Doppler velocity as large as $\pm$2 km s^{-1} appear inside the enlarged region at the boundaries of granules, where the convective flow shows converging motions to the intergranular lanes.

The jet threads are developed as a fan with footpoints following a brighter line in the south of the well-visible threads

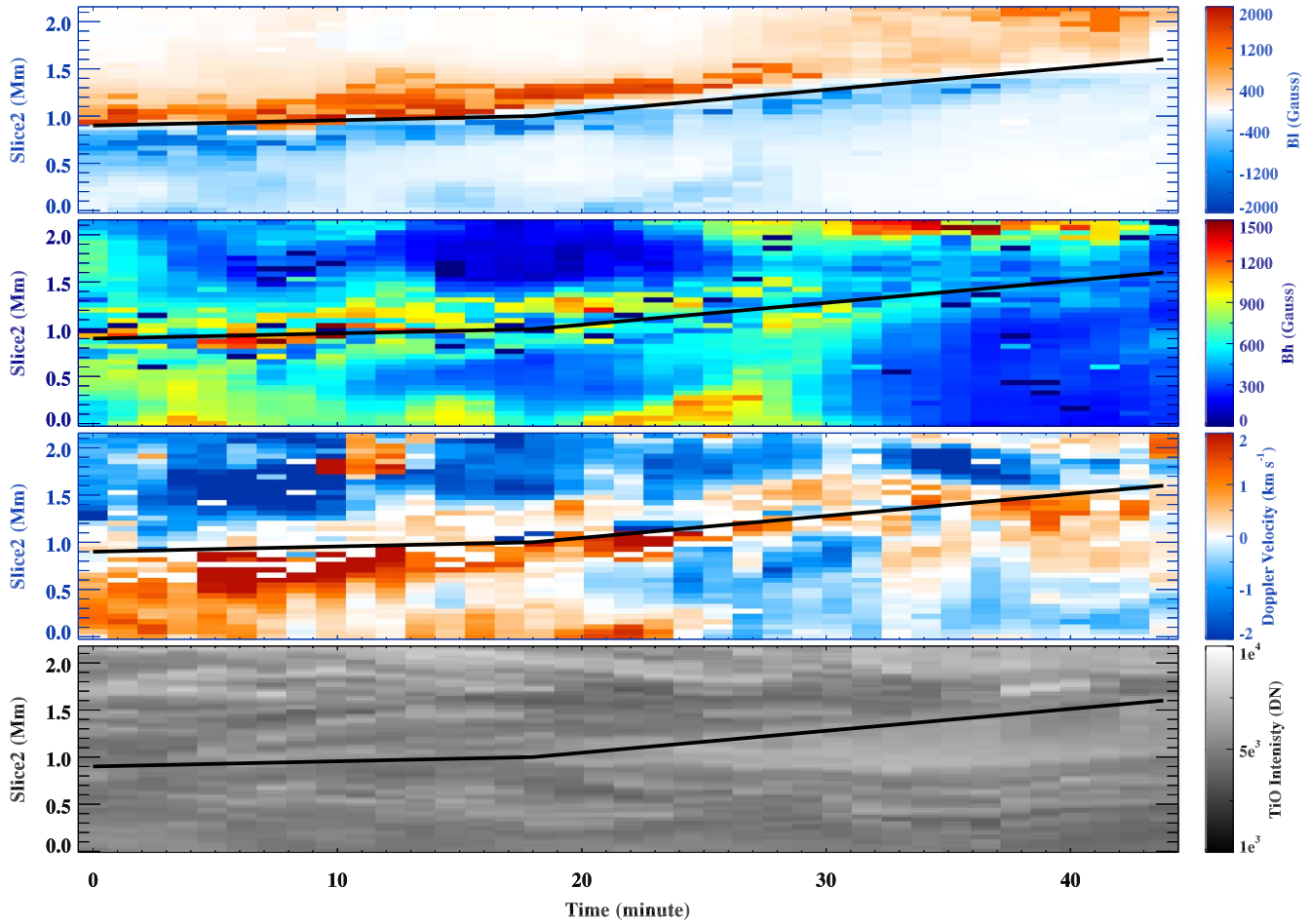

Figure 8. Same as Figure 7, but for Slice 2. The black curve is plotted to represent the place in between the opposite longitude magnetic field and is plotted in the other three panels for reference.

in Hα line center (Figure 5, top panels). We concentrate our study on some of them. They correspond to the inversion line of the magnetic field (also the intergranular lanes) indicated by the red arrows in Figure 5. From the distribution of the above four parameters around the intergranular lanes, we notice that there are two regions (FOV1 and FOV2 as annotated in Figure 6) with distinct properties. In the region of FOV1, the magnetic field is dominated by B_h and the Doppler velocity at the intergranular lanes is blueshift dominated, while in the region of FOV2, the magnetic field is dominated by B_l and the Doppler velocity at the intergranular lanes is redshift dominated. The intergranular lanes usually have Doppler redshift (downflows) and longitude-dominated magnetic field at the quiet region while Doppler velocity and the magnetic field may have different features if there is flux emergence or energy release. Flux emergence on a granular scale observed by the New Vacuum Solar Telescope with high resolution (Shen et al. 2022) shows that the flux emerges as a dark lane and the associated surge has footpoints closely rooted in these intergranular lanes, exhibiting horizontal magnetic field and convergence flows. Elongated horizontal magnetic field has also been found during the emergence of the top of small loops (Guglielmino et al. 2018). For understanding their different roles for driving the recurrent fan-like jets, we do a time–distance investigation along Slices 1 and 2 as labeled in the bottom panels of Figure 6; both of the slices pass through the intergranular lanes in the vicinity of the fan-like jets.

3.3. Magnetic Cancellation

Time–distance images of Slices 1 and 2 are shown in Figures 7 and 8, respectively. The longitude magnetic field, horizontal magnetic field, Doppler velocity, and TiO intensity are displayed from top to bottom.

In Figure 7, the black curve is selected, according to the maximum B_h at each time step, to represent the intergranular lanes. The horizontal field is always high at the intergranular lanes, where opposite polarities are identified and the Doppler velocity shows a blueshift. The TiO intensity near the black curve is higher than its surroundings at most time steps, indicating the existence of heating at the photosphere.

In Figure 8, the black curve is selected manually to represent the intergranular lanes. From the first two rows, an impulsive cancellation process is apparent, i.e., the opposite polarities of B_l decrease, while the B_h increases intermittently. More evidence is found from the bottom two rows, where the enhancement of TiO images is identified near the black line and the Doppler velocity is redshift dominated there, giving a hint of magnetic cancellation downflow. The feature of downflow at the photosphere indicates that the reconnection happens above, which is common for the reconnection between longitude-component-dominated magnetic fields with opposite polarities. The impulsive cancellation is also consistent with the relatively large convective flow as mentioned above. The TiO intensity at the intergranular lane is not always bright, as the magnetic cancellation happens intermittently and the

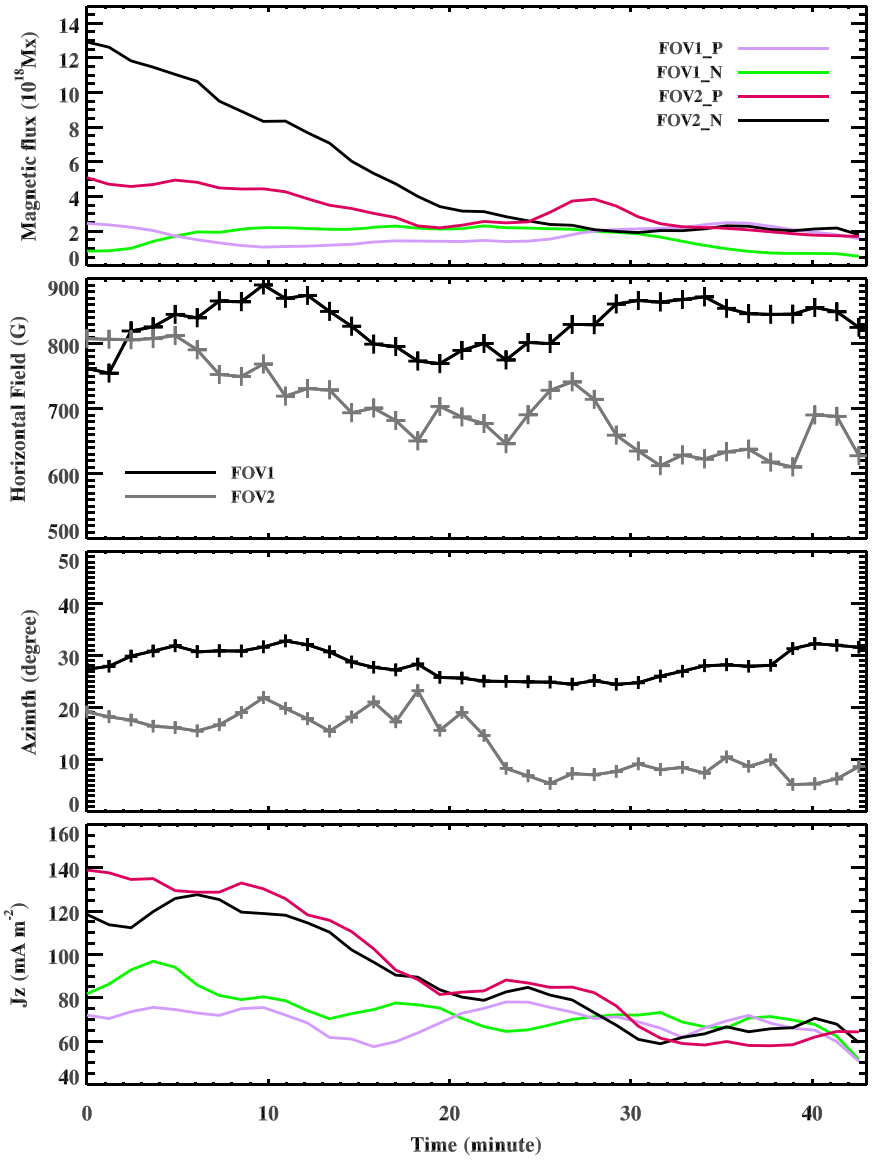

Figure 9. Evolution of magnetic features at two regions as shown in Figure 6. From top to bottom are magnetic flux (positive and absolute value of negative), mean horizontal field, mean azimuth, and mean vertical current density (positive and absolute value of negative), respectively. The legends of different colors in the panels of magnetic flux and horizontal magnetic field are also applicable to the vertical current density and the azimuth, respectively.

energy release might also be disturbed by other activities (such as flux emergence or granule convection adjacent).

3.4. Temporal Evolution of Magnetic Field

To show the overall magnetic properties at the above-mentioned two regions of FOV1 and FOV2, four parameters are calculated. Evolution of the magnetic flux, the mean horizontal field, the mean azimuth, and the mean vertical current density are plotted from top to bottom panels in Figure 9. The absolute values of magnetic flux of positive and negative B_l in the two regions are shown in the first panel. Both magnetic fluxes of positive and negative polarities in FOV2 show a decay tendency (from -1.3×10^{19} Mx to -2×10^{18} Mx for negative flux and from 5×10^{18} Mx to 2×10^{18} Mx for positive flux), while they do not change much in FOV1. The mean value of B_h and azimuth of vector magnetic field in FOV1 show variations with time but have less intermittent change compared to the ones in FOV2. The horizontal magnetic field in FOV2 after reconnection is more parallel to the intergranular lanes, which are almost along the x-axis as shown in Figure 6. Both positive and negative vertical current density have an apparent decrease in FOV2 (from 140 to 60 mA m^{-2} for positive current density and from -120 to -60 mA m^{-2} for negative current density), while slight decay is found in FOV1.

In general, the magnetic cancellation is apparent in FOV2, while no clear evidence is found in FOV1. As the fields with opposite polarities have been identified at the intergranular lanes in Figure 7, the magnetic cancellation is preferred to happen. However, as the magnetic flux in FOV1 shows a slight increase for the positive polarity around 17:30UT, magnetic flux emergence is also suspected to happen at the intergranular lanes, where the Doppler velocity is blueshifted as demonstrated in Figure 7. Such magnetic emergence might be cospatial with the magnetic cancellation and hence weaken the performance of the latter one in FOV1.

4. Discussion and Conclusion

In this work, the magnetic origin of fan-like jets on the scale of intergranules is studied in detail for the first time. Magnetic cancellation near the intergranular lanes is suggested to be responsible for the recurrent jets. Horizontal converging flows are identified, driving the repeatedly occurring cancellation. Doppler velocity of redshift is found to exist at the location of intergranular lanes, indicating the reconnection downflow at the photosphere.

The intergranular lanes are located inside the region in between a group of sunspots, on one side of which there is a well-developed and isolated sunspot with umbra and penumbra. It is different from the LB that commonly appears inside the umbra of a sunspot separating the umbra into two spots. Although the fan-like jets are not associated with an LB, the regions in between the sunspots show similar features, i.e., weak magnetic field with the same polarity compared to the ambient magnetic field. Comparing to the LB-originated fan-like jets in S09, the jets studied in our case have a larger length in scale (10 Mm vs. 1.3 Mm in S09) and a similar speed (42 km s^{-1} vs. 40 km s^{-1} in S09). The photospheric footpoints also show a high value of Doppler velocity (2 km s^{-1} vs. 0.73 km s^{-1} in S09) at the places where magnetic cancellation happens. No large-scale vertical current sheet like that shown in S09 is found in our case, but magnetic flux cancellation is identified. Therefore, a convection-driven magnetic cancellation on granular scales rather than a large-scale flux rope emergence is more plausible to be the main cause of the magnetic reconnection at the footpoint that is responsible for the recurrent fan-like jets in this study.

The convective nature at the photosphere in our case is consistent with the simulation results of the LB in T15, where the convective upflow transports horizontal fields to the surface layers and creates a magnetic configuration favorable for magnetic reconnection. The intergranular lanes that generate fan-like jets have convective flows with mixed magnetic polarities. The flows play a role in squashing the opposite polarities and make the reconnection happen. The intergranular lanes are occupied with strong magnetic field on the magnitude of the active region either along the line of sight (LOS) or at the horizontal plane. This finding is complementary to the picture of granule kinematics in the quiet region, which assumes a B_l-dominated magnetic field at the intergranular lanes. The Doppler velocity of the convective flow might be covered by the reconnection outflow, while the horizontal velocity (V_x in T15) in our case is as fast as 4 km s^{-1}, larger than the observation results (Toriumi et al. 2015b) from Hinode but consistent with the simulation one.

We thank the anonymous referee for the valuable suggestions to greatly improve our paper. We acknowledge fruitful discussion with Prof. Pengfei Chen, Prof. Hui Tian, Dr. Zhi Xu, and Dr. Ying Li. J.Z. was a visiting postdoc at HAO, supported by the Chinese Scholarship Council (CSC No. 201704910457). This work is also supported by Chinese Academy of Science Strategic Pioneer Program on Space Science, grant Nos. XDA15052200, XDA15320103, and XDA15320301, and by National Natural Science Foundation of China, grant Nos. U1731241 and 11503089. BBSO operation is supported by NJIT and US NSF AGS-1821294 grant. GST operation is partly supported by the Korea Astronomy and Space Science Institute and the Seoul National University. X.Y. and K.A. acknowledge support from US NSF AST-2108235 and NASA 80NSSC20K0025 grants.

ORCID iDs

Jie Zhao https://orcid.org/0000-0003-3160-4379
Jiangtao Su https://orcid.org/0000-0002-5152-7318
Xu Yang https://orcid.org/0000-0002-3238-0779
Hui Li https://orcid.org/0000-0003-1078-3021
Brigitte Schmieder https://orcid.org/0000-0003-3364-9183
Kwangsu Ahn https://orcid.org/0000-0001-7532-2635
Wenda Cao https://orcid.org/0000-0003-2427-6047

References

Ahn, K., & Cao, W. 2019, in ASP Conf. Ser. 526, Solar Polarization Workshop 8, ed. L. Belluzzi et al. (San Francisco, CA: ASP), 317
Ahn, K., Cao, W., Shumko, S., & Chae, J. 2016, AAS/Solar Physics Division Meeting, 47, 2.07
Archontis, V., Tsinganos, K., & Gontikakis, C. 2010, A&A, 512, L2
Asai, A., Ishii, T. T., & Kurokawa, H. 2001, ApJL, 555, L65
Bai, X., Socas-Navarro, H., Nóbrega-Siverio, D., et al. 2019, ApJ, 870, 90
Cao, W., Goode, P. R., Ahn, K., et al. 2012, in ASP Conf. Ser. 463, Second ATST-EAST Meeting: Magnetic Fields from the Photosphere to the Corona, ed. T. R. Rimmele et al. (San Francisco, CA: ASP), 291
Cao, W., Gorceix, N., Coulter, R., et al. 2010, AN, 331, 636
De Pontieu, B., Polito, V., Hansteen, V., et al. 2021, SoPh, 296, 84
De Pontieu, B., Title, A. M., Lemen, J. R., et al. 2014, SoPh, 289, 2733
Guglielmino, S. L., Zuccarello, F., Young, P. R., Murabito, M., & Romano, P. 2018, ApJ, 856, 127
Handy, B. N., Acton, L. W., Kankelborg, C. C., et al. 1999, SoPh, 187, 229
Hou, Y., Zhang, J., Li, T., Yang, S., & Li, X. 2017, ApJL, 848, L9
Hou, Y. J., Li, T., Yang, S. H., & Zhang, J. 2016, A&A, 589, L7
Ichimoto, K., Lites, B., Elmore, D., et al. 2008, SoPh, 249, 233
Jiang, R. L., Fang, C., & Chen, P. F. 2012, ApJ, 751, 152
Leka, K. D., Barnes, G., & Crouch, A. 2009a, in ASP Conf. Ser. 415, The Second Hinode Science Meeting: Beyond Discovery-Toward Understanding, ed. B. Lites et al. (San Francisco, CA: ASP), 365
Leka, K. D., Barnes, G., Crouch, A. D., et al. 2009b, SoPh, 260, 83
Lites, B. W., Akin, D. L., Card, G., et al. 2013, SoPh, 283, 579
Louis, R. E., Beck, C., & Ichimoto, K. 2014, A&A, 567, A96
Pariat, E., Antiochos, S. K., & DeVore, C. R. 2009, ApJ, 691, 61
Robustini, C., Leenaarts, J., de la Cruz Rodriguez, J., & Rouppe van der Voort, L. 2016, A&A, 590, A57
Roy, J. R. 1973, SoPh, 28, 95
Scherrer, P. H., Schou, J., Bush, R. I., et al. 2012, SoPh, 275, 207
Schmieder, B., Joshi, R., & Chandra, R. 2021, arXiv:2111.09002
Schmieder, B., Mein, P., Simnett, G. M., & Tandberg-Hanssen, E. 1988, A&A, 201, 327
Shen, J., Xu, Z., Li, J., & Ji, H. 2022, ApJ, 925, 46
Shimizu, T., Katsukawa, Y., Kubo, M., et al. 2009, ApJL, 696, L66
Shimojo, M., & Shibata, K. 2000, ApJ, 542, 1100
Su, J. T., Ji, K. F., Cao, W., et al. 2016, ApJ, 817, 117
Takasao, S., Isobe, H., & Shibata, K. 2013, PASJ, 65, 62
Tian, H., Yurchyshyn, V., Peter, H., et al. 2018, ApJ, 854, 92
Toriumi, S., Cheung, M. C. M., & Katsukawa, Y. 2015a, ApJ, 811, 138
Toriumi, S., Katsukawa, Y., & Cheung, M. C. M. 2015b, ApJ, 811, 137
Wang, H., Liu, C., Ahn, K., et al. 2017, NatAs, 1, 0085
Yang, H., Lim, E.-K., Iijima, H., et al. 2019a, ApJ, 882, 175
Yang, S., Zhang, J., Jiang, F., & Xiang, Y. 2015, ApJL, 804, L27
Yang, X., Yurchyshyn, V., Ahn, K., Penn, M., & Cao, W. 2019b, ApJ, 886, 64
Yokoyama, T., & Shibata, K. 1996, PASJ, 48, 353
Zhang, J., Tian, H., He, J., & Wang, L. 2017, ApJ, 838, 2